Earth Planet. Sci. Lett. 637 (2024) 118737

Contents lists available at ScienceDirect

Earth and Planetary Science Letters

journal homepage: www.elsevier.com/locate/epsl

Long-lasting farside volcanism in the Apollo basin: Chang'e-6 landing site

Yuqi Qian [a,*], James Head [b], Joseph Michalski [a,*], Xing Wang [b,c], Carolyn H. van der Bogert [d], Harald Hiesinger [d], Lingzhi Sun [e], Wei Yang [f], Long Xiao [g], Xianhua Li [f], Guochun Zhao [a]

[a] Department of Earth Sciences & Laboratory for Space Research & NWU-HKU Joint Center of Earth and Planetary Sciences, The University of Hong Kong, Hong Kong, China
[b] Department of Earth, Environmental and Planetary Sciences, Brown University, Providence, RI, USA
[c] Key Laboratory of Lunar and Deep Space Exploration, National Astronomical Observatories, Chinese Academy of Sciences, Beijing, China
[d] Institut für Planetologie, Universität Münster, Münster, Germany
[e] Hawai'i Institute of Geophysics and Planetology, University of Hawai'i at Mānoa, Honolulu, HI, USA
[f] Key Laboratory of Earth and Planetary Physics, Institute of Geology and Geophysics, Chinese Academy of Sciences, Beijing, China
[g] Planetary Science Institute, School of Earth Sciences, China University of Geosciences, Wuhan, China

ARTICLE INFO

Editor: Dr. F. Moynier

Keywords:
Chang'e-6
Lunar sample return
Lunar farside volcanism
South Pole-Aitken basin
Apollo basin

ABSTRACT

A major lunar scientific question is the cause of the paucity of farside mare basalts. The South Pole-Aitken Basin (SPA) is the largest (2400×2050 km) and most ancient lunar impact basin. The Apollo peak-ring basin, the largest impact feature within the SPA, is located on its northeast edge in a transitional zone of crustal thickness and compositions. The Chang'e-6 (CE-6) mission, the first sample-return mission to the lunar farside, is targeted to land in the southern Apollo basin, sampling farside mare basalts with critical insights into early lunar evolution. In preparation for the CE-6 sample return, we conducted a comprehensive study of Apollo basin volcanism. We found that volcanic activity began in the Nectarian Period (~4.05 Ga) (cryptomaria) and continued into the Eratosthenian Period (~1.79 Ga). At least two Imbrian-aged episodes of eruptions occurred in the southern part of the Apollo basin where CE-6 is targeted to land. At ~3.35 Ga, low-Ti (~3.2 wt %) volcanism was active, and its products covered the entire low topographic region of the southern Apollo basin, between the inner and outer rings. Closely following its eruption at ~3.07 Ga, high-Ti basalts (~6.2 wt %) erupted close to the Chaffee S crater and flowed east with decreasing thickness until encountering proto-wrinkle ridges. In addition, volcanic activity in the region is significantly correlated with low crustal thickness, primarily thinned by the SPA and Apollo impact events. For regions of intermediate-thick crust (Oppenheimer crater), dikes stalled under the crater floor, spreading to form sills and a floor-fractured crater. For thin crust regions (Apollo basin interior), dikes erupted directly, forming extensive lava flows. In areas of thick highland crust, we see no evidence of extrusive activity or floor-fractured craters, suggesting that dikes there do not reach the surface and are intrusive. CE-6 samples returned from the unique geological setting will provide significant petrogenetic information to address further the paucity of farside mare basalts and the lunar nearside-farside dichotomy. To solve those scientific questions, the high-Ti mare region in south Apollo basin is recommended as the priority landing site.

1. Introduction

Lunar mare basalts are the products of mantle partial melting followed by magmatic ascent and eruption (Neal and Taylor, 1992). Approximately 18 % of the lunar surface is covered by mare (~16 %) and cryptomare (~2 %) deposits, contributing less than 1 % of the total volume of the crust (on the order of 10^7 km^3) (Whitten and Head, 2015). However, the distribution of lunar volcanism is not symmetrical in space (Nelson et al., 2014) and time (Hiesinger et al., 2011). Approximately 30 % of the nearside is covered by mare basalts and only a few large farside impact basins contain mare deposits (e.g., South Pole-Aitken, Moscoviense, Apollo, Schrodinger basins and Tsiolkovsky crater). This nearside-farside dichotomy, first recognized by Luna-3 at the dawn of the Space Age, and well recorded by modern datasets, not only included the distribution of volcanism, but also topography, surface morphology, elemental concentration, terranes and crustal thickness (Jolliff et al., 2000; Smith et al., 2010; Wieczorek et al., 2013). Nevertheless, no consensus has yet been reached to explain its origin. All existing models

---

* Corresponding authors.
E-mail addresses: yuqiqian@hku.hk (Y. Qian), jmichal@hku.hk (J. Michalski).

https://doi.org/10.1016/j.epsl.2024.118737
Received 17 September 2023; Received in revised form 10 March 2024; Accepted 22 April 2024

(Jutzi and Asphaug, 2011; Ohtake et al., 2012; Zhang et al., 2022) are limited to numerical simulations, due to the lack of confirmed farside samples, although some may be contained in meteorites or Apollo breccias (Calzada-Diaz et al., 2015; Garrick-Bethell et al., 2020).

The South Pole-Aitken (SPA) basin (centered at 53°S, 191°E) is the largest (2400×2050 km) and most ancient (~4.25 Ga) (Garrick-Bethell et al., 2020) definitive lunar impact basin (Fig. 1A). The SPA impact likely removed the anorthositic crust and excavated deep-seated materials down to ~100 km, even in the most conservative estimates (Potter et al., 2012). Located on the farside, with extensive deposits of potentially deep-sourced rocks, the SPA basin remains a critical target that can address the multiple nearside-farside conundra (Jolliff et al., 2021).

Chang'e-6 (CE-6), scheduled to launch in the middle of 2024, is China's second lunar sample-return mission following Chang'e-5 (CE-5). CE-6 has the same capability as CE-5 to collect 2 kg of lunar soils (Zhou et al., 2022), and will become the world's first farside sample-return mission. On the basis of the scientific value and engineering constraints, the area between 150 and 158°W and 41–45°S in the southern Apollo basin (Fig. 1B) has been selected as the landing region (Zeng et al., 2023).

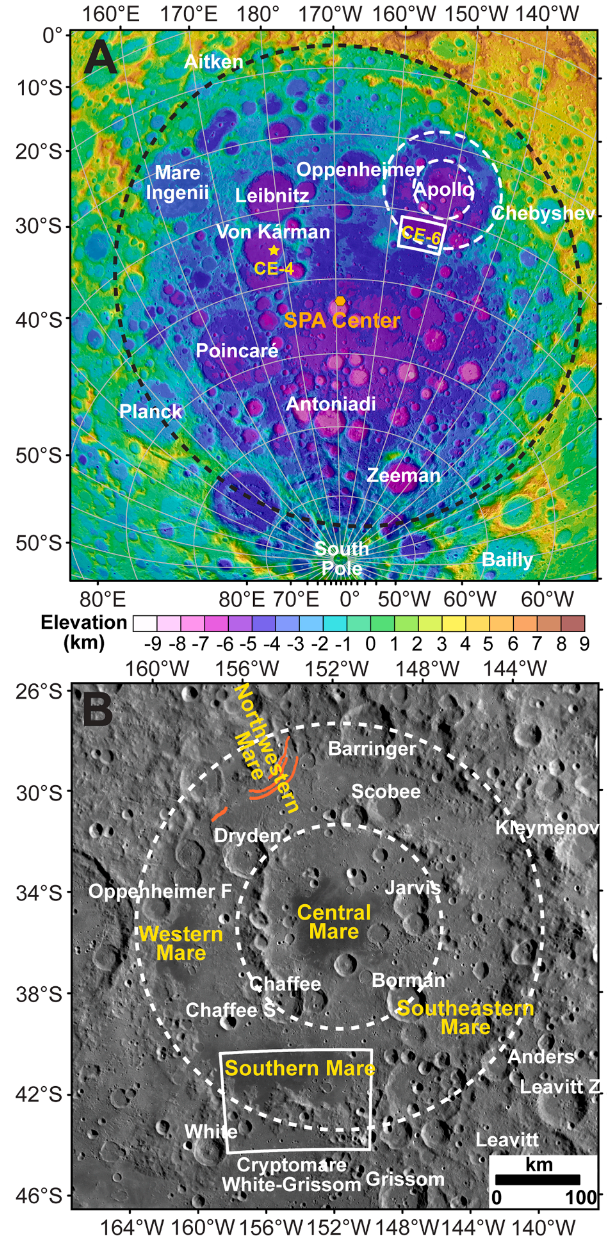

Fig. 1. Geological background of the Apollo basin. (A) Location of the Apollo basin in the northeast area of SPA. The black dashed line represents the outer ring of SPA. The white box represents the CE-6 landing region. The basemap is a LRO LOLA DEM overlain on a WAC image. (B) Apollo basin and related mare deposits. The white box represents the CE-6 landing region. The white dashed lines represent the Apollo basin rings. The red lines represent troughs. The basemap is a LROC WAC image.

The Apollo peak-ring basin (centered at 36.1°S, 208.3°E) is the largest impact feature within SPA, with a diameter of 247 km and 492 km for the inner and outer rings (Neumann et al., 2015) (Fig. 1B). It is located to the northeast of SPA, extending from its interior to rim (Fig. 1A), crossing distinct compositional zones (Moriarty and Pieters, 2018). Numerical modeling suggests that the Apollo impact was produced by a 40 km-diameter body impacting into a 20–40 km-thick crust at a speed of 15 km/s (Potter et al., 2018). This impact penetrated through the ejecta of SPA down to a depth of ~30 km, probably excavating sub-crustal materials and exposing them in the peak ring (Potter et al., 2018; Wang et al., 2024). After the formation of Apollo, the northwestern, western, central, southern, and southeastern parts of Apollo basin were flooded by mare basalts (Fig. 1B) (Ivanov et al., 2018). Due to landing safety guidelines, the mare plains in the north of the landing region and the cryptomare on the southern rim of Apollo basin have been shortlisted as candidate landing sites (Zeng et al., 2023) (Fig. 1B). All of them are products of farside volcanism, and thus CE-6 will highly likely collect basaltic soils from the farside.

Although there are a few studies of volcanism in SPA and the lunar farside (Haruyama et al., 2009; Pasckert et al., 2018; Pieters et al., 2001), the setting of mare volcanism associated with the Apollo basin has not yet been analyzed in detail. Here we report on a comprehensive study of the volcanic deposits and features within and around the Apollo basin, aiming to construct a complete volcanic history as a framework for understanding the geological context of the CE-6 samples and help to locate their key scientific meanings.

2. Materials and methods

2.1. Morphology and topography

Lunar Reconnaissance Orbiter (LRO) Wide-Angle-Camera (WAC) data were used to analyze the geomorphology of the Apollo basin (Robinson et al., 2010). A global mosaic, comprised of over 15,000 images acquired between Nov. 2009 and Feb. 2011, with a spatial resolution of 100 m/pixel, is suitable to study large-scale features. Kaguya Terrain Camera (TC, 10 m/pixel) data (Haruyama et al., 2008) were used as a supplement to the WAC images for characterizing small-scale volcanic features. The TC Morning Map and Ortho Map products were used; they were obtained in low-sun early and late solar illumination conditions.

All topographic analyses were based on SLDEM2015, a digital elevation model (DEM) product generated via co-registration of Lunar Orbiter Laser Altimeter (LOLA) data and stereo-derived TC DEMs (Barker et al., 2016). SLDEM2015 covers latitudes between 60°S to 60°N, with a spatial resolution of 512 pixels per degree (~59 m/pixel) and a vertical resolution of ~3–4 m. Additionally, the LOLA DEM (Smith et al., 2010) was used to further characterize the high-latitude region (60°S-90°S) where there is no SLDEM2015 coverage. The LOLA DEM has a vertical precision of ~10 cm and a spatial resolution of 256 pixels per degree (~118 m/pixel).

2.2. Composition

The Multiband Imager (MI) is another main payload onboard Kaguya (Haruyama et al., 2008). Its ultraviolet-near infrared (415, 750, 900, 950, 1001 nm) sensor data were used to quantitively analyze the surface composition (TiO_2 and FeO, reported in wt %) (Fig. S1), with a resolution of 20 m/pixel (Ohtake et al., 2008). TiO_2 abundance was calculated utilizing the approach of Otake et al. (2012),

$$\theta_{Ti} = arctan\left\{\frac{\frac{R_{415}}{R_{750}} - 0.208}{R_{750} + 0.108}\right\};$$

$$TiO_2(wt.\ \%) = arctan\left\{\frac{\frac{R_{415}}{R_{750}} - 0.208}{R_{750} + 0.108}\right\}$$

and FeO abundance was calculated by the method of Lemelin et al. (2015),

$$\begin{aligned} \theta_{Fe1} &= -arctan\left\{\frac{\frac{R950}{R750} - 1.39}{R750 - 0.04}\right\}; \\ \theta_{Fe2} &= 0.0656e^{3.6681*\theta_{Fe1}}; \\ FeO\ (wt.\%) &= 1.0708*\theta_{Fe2} - 0.3986 \end{aligned}$$

where R_{415}, R_{750}, R_{950} represent reflectance at 415, 750, and 950 nm, respectively. For each mare unit, their mean TiO_2 and FeO abundance is computed (Table 1), and further classified into very low-Ti (<1 wt %), low-Ti (1–6 wt %), and high-Ti (>6 wt %) basalts (Neal and Taylor, 1992).

The Ultraviolet/Visible (UVVIS) camera (200 m/pixel) onboard Clementine has bands identical to MI (Nozette et al., 1994). Thus, the UVVIS color composite map (Red: 750/415 nm; Green: 750/1000 nm; Blue: 415/750 nm) is used to help subdivide geological units. In this map, red represents low-titanium content or high-glass content, green is sensitive to iron abundance, and blue usually reflects high-titanium content (Pieters et al., 1994).

2.3. Spectral analysis

To analyze the mineralogy (CPX=clinopyroxene, OPX=orthopyroxene, PYX=pyroxene, OLV=olivine, PLG=plagioclase) of mare units, we extracted spectra from small-fresh craters in Moon Mineralogy Mapper (M^3) data and analyzed them with the radiative transfer model. M^3 was a push-broom imaging spectrometer onboard Chandrayaan-1, operating in a wavelength range of 0.43–3.0 μm (85 channels) that covers the diagnostic absorption feature of major lunar silicate minerals (Pieters et al., 2009). The data used are OP2C2 reflectance data with a spatial resolution of 140×280 m/pixel, underwent radiometric (Green et al., 2011), geometrical (Boardman et al., 2011), thermal (Clark et al., 2011), photometrical (Besse et al., 2013), and ground truth (Isaacson et al., 2013) calibrations. In total, 90 spectra from small-fresh craters were selected to represent major geological units (Fig. S2). Their detailed information (coordinates, ID, values, etc.) can be found in Table S3 and S4. An example of how to extract spectra from small-fresh craters is shown in Fig. S3; only their spectra were extracted to acquire high signal-to-noise ratio data that less affected by space weathering. Utilizing the spectra of the entire area covered by the mare units would inevitably include areas that are heavily space weathered (most of the area) or covered by exotic impact ejecta (e.g., bright rays, Fig. 2A); therefore, this approach was not used here.

All spectra were processed by the method described by Qian et al. (2023). Each spectrum was smoothed by the Savitzky-Golay filter (Fig. S4). The continuum was removed by the convex-hull method. The band center for Band I and II was calculated by finding the local minima between 800 and 1200 nm and 1700–2500 nm in the continuum-removed spectra. The band center of typical lunar minerals (Mg-OPX, Fe-OPX, Low-Ca CPX, High-Ca CPX, Wo50-PYX) from Klima et al. (2007) was computed for comparison with the mare units. The quantitative abundance of major minerals (CPX, OPX, OLV, and PLG) of each spectrum was estimated by the lookup table technique (reported in vol %) following the same procedure of Sun and Lucey (2021) based the Hapke radiative transfer modeling (Hapke, 1981) (Details in Text S1). According to sensitivity tests, this approach has an accuracy of 3 and 6 vol % for estimating the abundance of mafic minerals and plagioclase. Finally, for each unit, their major mineral abundances were computed by averaging the abundance from all extracted spectra (Table 1).

Table 1
Absolute model ages and composition of mare units in the study area.

	Model Age (Ga)	FeO (wt %)	TiO_2 (wt %)	CPX (vol %)	OPX (vol %)	OLV (vol %)	PLG (vol %)
Northwestern Mare	$1.79^{+0.26}_{-0.26}$	13.1 ± 0.8	2.2 ± 0.5	23.6 ± 3.8	23.3 ± 12.0	1.9 ± 2.6	51.2 ± 15.0
Central Mare	$2.01^{+0.10}_{-0.10}$	19.0 ± 0.6	6.5 ± 1.0	29.7 ± 6.7	23.9 ± 2.9	7.3 ± 2.5	39.1 ± 5.0
Western Mare	$2.12^{+0.14}_{-0.14}$	16.7 ± 0.6	3.2 ± 0.6	27.8 ± 5.8	27.7 ± 4.9	0.0 ± 0.0	44.4 ± 5.5
Southeastern Mare	$2.72^{+0.20}_{-0.24}$	18.0 ± 0.6	6.2 ± 0.9	30.5 ± 6.9	21.6 ± 3.1	1.9 ± 2.6	46.0 ± 7.9
Southern Mare 1	$3.07^{+0.07}_{-0.08}$	18.3 ± 0.7	6.2 ± 1.0	33.8 ± 9.9	23.3 ± 5.9	3.6 ± 2.8	39.3 ± 11.7
Southern Mare 2	$3.34^{+0.04}_{-0.06}$	16.6 ± 1.0	3.2 ± 0.5	25.4 ± 6.9	30.1 ± 6.6	0.9 ± 3.0	43.6 ± 14.4
Cryptomare Type 1 Area	/	14.8 ± 0.8	2.1 ± 0.4	20.9 ± 5.2	20.1 ± 6.2	0.4 ± 1.3	58.6 ± 9.0
Cryptomare Type 2 Area	$4.05^{+0.01}_{-0.01}$	13.1 ± 0.7	1.4 ± 0.3	11.0 ± 5.2	25.2 ± 6.8	0.0 ± 0.0	63.8 ± 3.2

2.4. Crater size-frequency distribution measurement

Crater size-frequency distribution (CSFD) measurements were made to obtain the absolute model ages (AMAs) of the mare units after Hiesinger et al. (2023) and references therein. The crater counting areas are shown in Fig. S5; only areas without heavy contamination of secondary craters, deformation by wrinkle ridges, or disruption by volcanic landforms were selected for counting. For each unit, CraterTools (Kneissl et al., 2011) was used to measure the diameters of primary craters on TC Morning Map. In total, 43,194 craters were measured. Then, Craterstats (Michael et al., 2016; Michael and Neukum, 2010) was used to fit the AMAs (Fig. S6, Table 1) via Poisson timing analysis, employing the production function of Neukum et al. (2001) and the chronology function of Yue et al. (2022) calibrated by CE-5 samples. Additional fits were made using the chronology function of Neukum et al. (2001) for easier comparison with previous studies (Table S1, S2).

3. Results

Low-albedo mare basalts are widespread in the study area, associated with diverse volcanic features. They were identified in the northwestern, western, central, southern, and southeastern parts of Apollo basin (Ivanov et al., 2018; Pasckert et al., 2018) and as cryptomare (Whitten and Head, 2015) on its south rim (Fig. 1B). Based on their locations, they are designated as Northwestern Mare, Western Mare, Central Mare, Southern Mare, Southeastern Mare, and Cryptomare White-Grissom.

3.1. Northwestern Mare

The Northwestern Mare is an elongated NW-SE striking mare unit

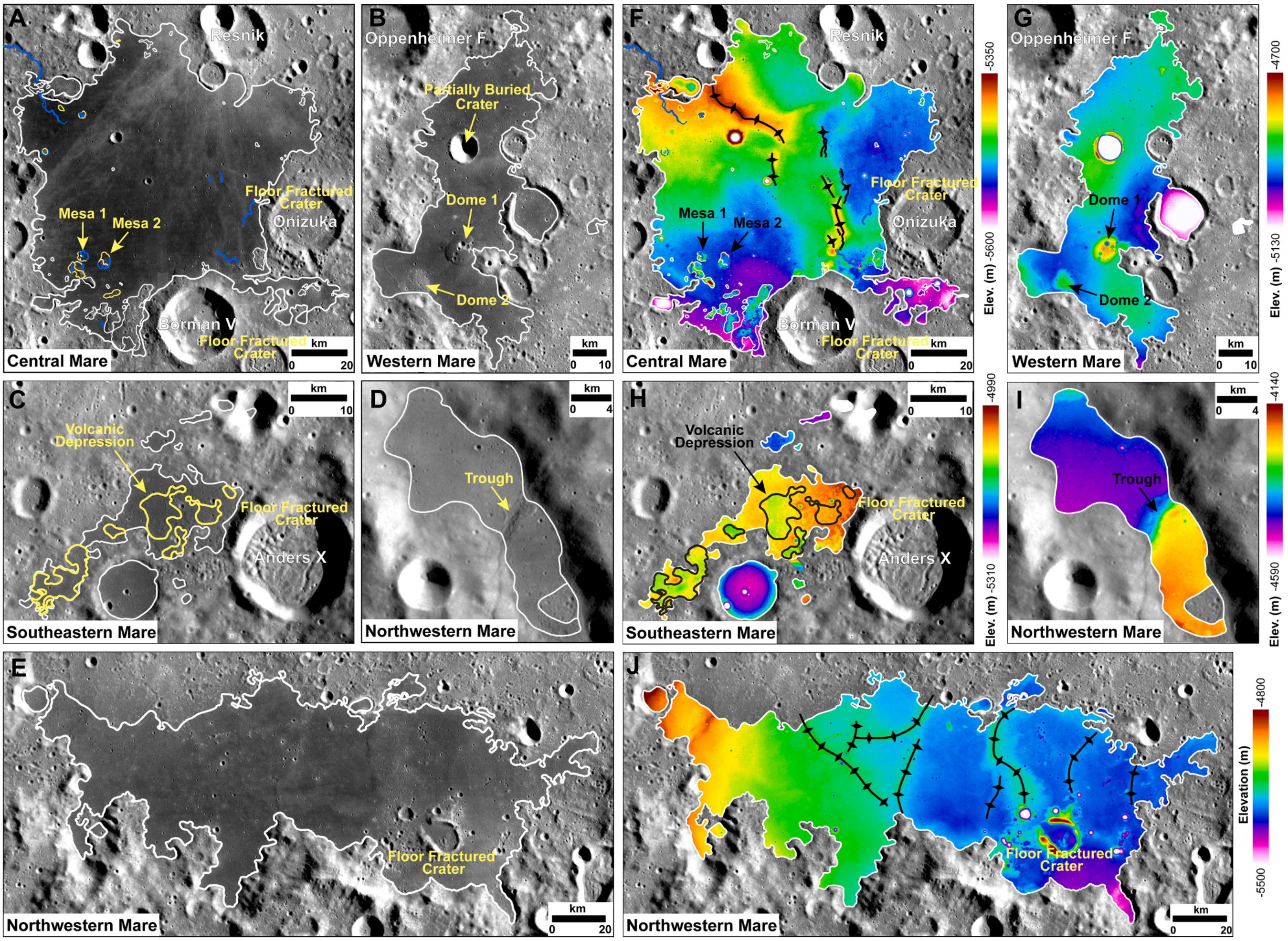

Fig. 2. Mare deposits and their elevations in the Apollo basin. (A, F) Central Mare. The blue and yellow lines indicate sinuous rilles and volcanic mesas. (B, G) Western Mare. (C, H) Southeastern Mare. The yellow/black lines indicate volcanic depressions. (D, I) Northwestern Mare. (E, J) Southern Mare. The white lines indicate mare boundaries. The black lines in (F, J) indicate wrinkle ridges. The basemaps are LROC WAC images (A-E) and SLDEM2015 overlain on LROC WAC images (F-J).

with an area of ~176 km^2 (Fig. 2D). The distribution of the Northwestern Mare is restricted to a radial secondary chain valley associated with the Apollo basin. Three long parallel troughs (55–85 km in length) are distributed close to the Northwestern Mare (Fig. 1B), including one crossing its middle (Fig. 2D). The mean elevation of Northwestern Mare is −4396 m. Its southern part (−4230 m) is much higher than the northern part (−4475 m) (Fig. 2I), likely later deformed (~245 m) by the trough formation.

The Northwestern Mare is a type of low-Ti basalt (2.2 ± 0.5 wt %) (Neal and Taylor, 1992) with low FeO abundance (13.1 ± 0.8 wt %) (Table 1). It has diagnostic pyroxene absorptions at 1 and 2 μm (Fig. 3A). Low-Ca CPX is the dominant type (Fig. 3B). Spectral unmixing indicates that the Northwestern Mare has 23.6 ± 3.8 vol % CPX, 23.3 ± 12.0 vol % OPX, 1.9 ± 2.6 vol % OLV, and 51.2 ± 15.0 vol % PLG. In addition, CSFD measurements suggest the Northwestern Mare has an AMA of $1.79^{+0.26}_{-0.26}$ Ga. It is the youngest mare within the Apollo basin.

3.2. Central Mare

The Central Mare has an area of ~8007 km^2 (Fig. 2A). Abundant bright rays cover its northern part, radiating from Resnik crater to the northeast, indicating a post-mare age (Fig. 2A). The mean elevation of the Central Mare is −5481 m (Fig. 2F). An elevated arc-shaped region in the middle is occupied by wrinkle ridges. The northeast and southwest parts of the Central Mare have the lowest elevation (~−5570 m) and the northwest has the highest elevation (~−5350 m).

The Central Mare is composed of high-Ti basalts. It has the highest TiO_2 (6.5 ± 1.0 wt %) and FeO (19.0 ± 0.6 wt %) abundances among all investigated mare units (Table 1). It has distinctive pyroxene absorptions at 1 and 2 μm, with band center close to low-Ca CPX (Fig. 3). M^3 spectra unmixing indicates that it has the highest mafic mineral abundance (CPX, 29.7 ± 6.7 vol %; OPX, 23.9 ± 2.9 vol %; OLV, 7.3 ± 2.5 vol %). CSFD measurements indicate that it has an AMA of $2.01^{+0.10}_{-0.10}$ Ga.

Abundant volcanic landforms occur within the Central Mare, including volcanic mesas and sinuous rilles (Fig. 2A), mostly concentrated at its edge. The two most prominent mesas are shown in Fig. 4AD (i.e., Mesa 1 and Mesa 2). Most of the surface of these two mesas has a composition indistinguishable from the surrounding mare (Fig. 4CF), but they also contain nonmare materials with extremely low FeO abundance. Topographic profiles derived across Mesa 1 (A'-A'') and Mesa 2 (B'-B'') are displayed in Fig. S8AB. The tops of both mesas are relatively flat. Mesa 1 (~ −5475 m) is 45 m higher than the mare surface, with the topography decreasing from west to east (Fig. 4B, S8A). The southwest part of Mesa 2 appears closely related to nonmare materials (Fig. 4F). The elevation is high in this nonmare part but decreases and becomes relatively flat in the northeastern basaltic part (Fig. 4E, S8B). Nearly all mesas in the basin are closely related to sinuous rilles and graben (Fig. 4AD), strongly supporting their volcanic origin.

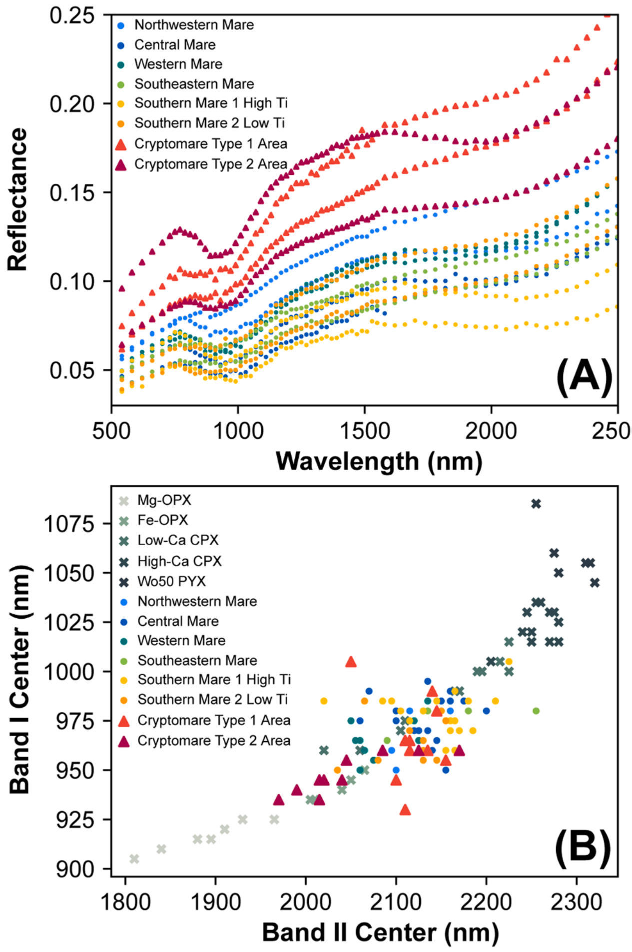

Fig. 3. Spectroscopy of mare units. (A) M^3 spectra of all mare units. (B) Band center of all mare units together with typical lunar minerals from Klima et al. (2007), including Mg-OPX, Fe-OPX, Low-Ca CPX, High-Ca CPX, and Wo50-PYX.

Abundant sinuous rilles (Fig. 2A) are distributed in the northwest and southeast parts of the Center Mare, with the longest length of ~55 km.

3.3. *Western Mare*

The Western Mare is a N-S elongated mare unit with an area of ~2501 km^2 (Fig. 2B). An 8.7 km-diameter crater, whose rim and exterior ejecta are embayed by maria, is located in the northern part of the Western Mare (Fig. 2B). The surface of the Western Mare is very flat (mean elevation of −4964 m), with slightly decreasing elevation from north to south.

The Western Mare is made up of low-Ti basalts (3.2 ± 0.6 wt %) with a FeO abundance of 16.7 ± 0.6 wt % (Table 1). It has prominent pyroxene absorptions at 1 and 2 μm, with a composition close to low-Ca CPX (Fig. 3). The Western Mare has 27.8 ± 5.8 vol % CPX, 27.7 ± 4.9 vol % OPX, 44.4 ± 5.5 vol % PLG, and no detectable olivine. CSFD measurements were used to obtain the model age of the Western Mare, which indicates that it erupted at $2.12^{+0.14}_{-0.14}$ Ga in the Eratosthenian Period.

Two domes are found in the southern Western Mare, denoted Dome 1 and 2 (Fig. 2B). Dome 1 is a quasi-circular feature (~8 × 10 km, Fig. 4G), with a composition similar to the surrounding mare. The highest point of Dome 1 is ~205 m higher than the mare. Five major craters were identified on Dome 1. Two of them may be collapsed volcanic vents (Fig. 4G, red-dashed circles) without pronounced raised rims (Fig. S8C). The other three craters, with apparent raised rim crests, are more likely to be impact craters (Fig. 4G, yellow-dashed circles). Dome 2 is a more circular feature (7.3 km in diameter) with the highest point ~120 m higher than the mare. It has a higher crater density (Fig. 4J) and lower TiO_2 abundance (~1.2 %, Fig. 4L) than the Western Mare, indicating that its formation predates the hosting mare. The diameter-height ratio of these two domes falls in the middle of mare domes generally interpreted to be related to mare volcanism (Head and Gifford, 1980). However, for Dome 1, the presence of highland material in the near-surface substrate, and its adjoining kipuka of highland material suggest that it may be a mare-mantled kipuka, rather than a construction feature (Class 5 and 6 domes of Head and Gifford, 1980). Dome 2 lacks the large central pit crater vent structure typical of effusive mare domes, and its position so close to the edge of the highland hints at the possibility that it may be an earlier-formed mare kipuka, embayed by later volcanic plains. At least five sinuous features were found on Dome 2 (Fig. 4J); four of them originate from the middle of the dome and extend outward. There are several off-summit irregular depressions that may be small volcanic pit craters. The origin of the sinuous features, and their relationship to the candidate pit craters is currently unclear. One possibility for the central dome-crossing sinuous feature is that it is a broad fracture caused by subsidence of early mare material that was draped over a now-buried highland kipuka.

3.4. *Southeastern Mare*

The Southeastern Mare is composed of several separate mare patches with a total area of ~457 km^2 (Fig. 2C). The mean elevation of the Southeastern Mare is −5116 m (Fig. 2H). There are at least six shallow depressions identified within the largest patch of the Southeastern Mare. The most prominent depression has a depth of ~27.5 m below the mare surface.

The Southeastern Mare consists of high-Ti basalts (6.2 ± 0.9 wt %) with an FeO abundance of 18.0 ± 0.6 wt % (Table 1). Low-Ca pyroxene is the main mafic mineral according to the extracted M^3 spectra (Fig. 3). Based on spectral unmixing, it has 30.5 ± 6.9 vol % CPX, 21.6 ± 3.1 vol % OPX, 1.9 ± 2.6 vol % OLV, and 46.0 ± 7.9 vol % PLG. The identical composition of the depressions and the mare surface, and their irregular shapes suggest that they are formed in the same eruption phase. CSFD measurements indicate that the Southeastern Mare has an AMA of $2.72^{+0.20}_{-0.24}$ Ga.

3.5. *Southern Mare*

The Southern Mare, the unit that CE-6 will most likely land on (Zeng et al., 2023), is a W-E elongated mare unit with a total area of ~9329 km^2 (Fig. 2E). The ejecta from the Chaffee S crater clearly overlies the northwestern Southern Mare, indicating a post-mare age (Fig. 5A). Wrinkle ridges are prominent linear features on the mare surface, with a dominant orientation of N-S (Fig. 5A). The mean elevation of the Southern Mare is ~5178 m, decreasing from west to east over ~300 m (Fig. 2J). A topographic profile (A-A') is shown in Fig. 5B. At least five wrinkle ridges (i.e., WR1 to WR5) occur across the profile line. The topography of the Southern Mare is significantly affected by their occurrence. Their formation appears to deform and raise the mare surface for at most ~100 m (Fig. 5B).

The eastern Southern Mare has a slightly higher albedo than the west (Fig. 6B), hinting that their composition might be distinct. This difference is much more clearly seen in the elemental abundance maps (Fig. 6ACD): the western part contains more FeO and TiO_2 than the east. This distinctive difference in composition suggests that they are the products of two remarkably different eruptions. We therefore further subdivided the Southern Mare into Southern Mare 1 (western part) and 2 (eastern part) (Fig. 6). Southern Mare 1 has a TiO_2 abundance of 6.2 ± 1.0 wt % and FeO abundance of 18.3 ± 0.7 wt %, much higher than Mare 2 (3.2 ± 0.5 wt % TiO_2 and 16.6 wt % FeO). Southern Mare 2 (43.6 ± 14.4 vol %) is richer in PLG than Mare 1 (39.3 ± 11.7 vol %), which

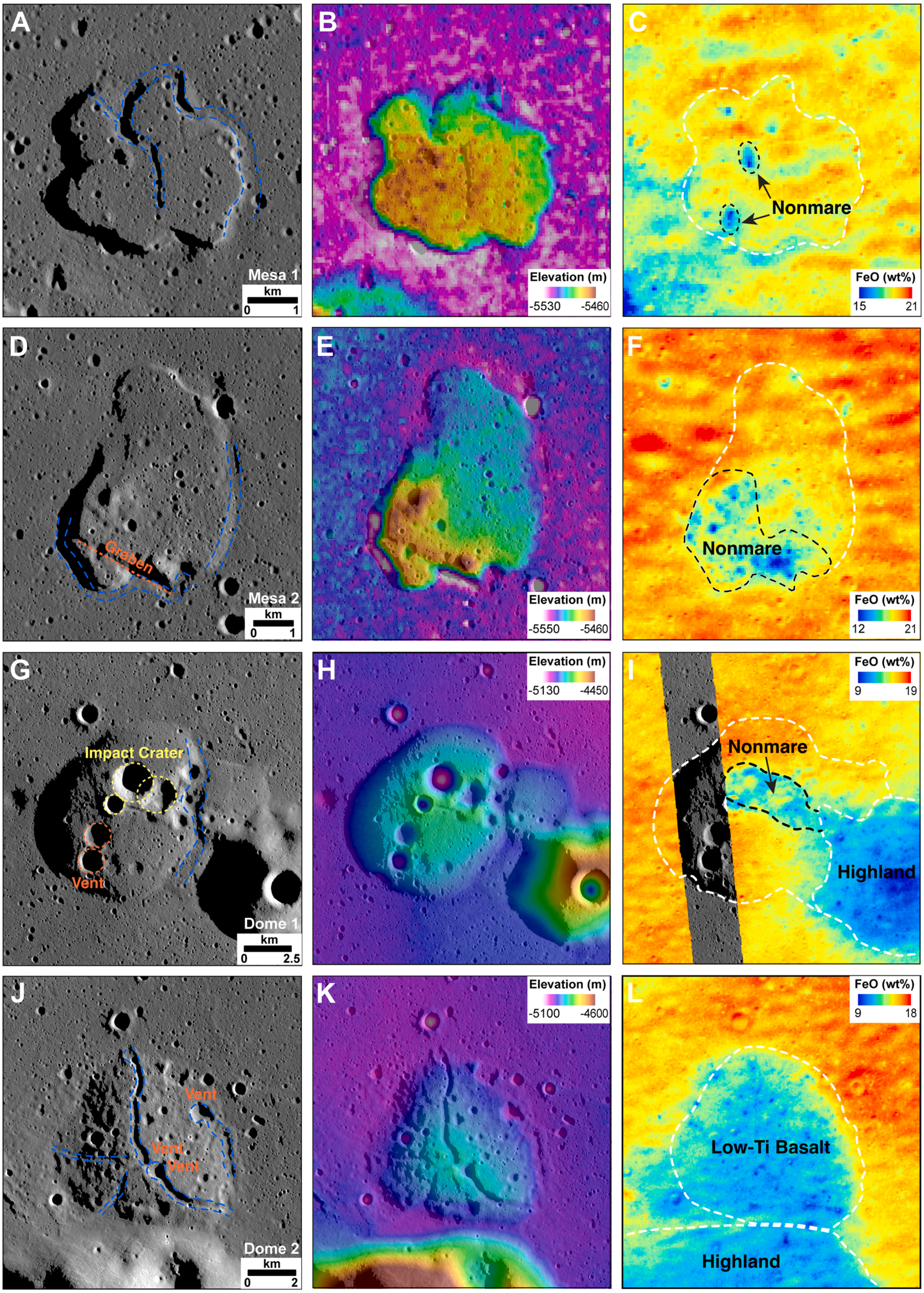

Fig. 4. Volcanic mesas and domes in the Apollo basin. (A-C) Mesa 1. (D-F) Mesa 2. (G-I) Dome 1. (J-L) Dome 2. The basemaps of the 1st, 2nd, and 3rd columns are TC Morning Map, SLDEM2015 overlain on TC Morning Map, and Kaguya MI FeO images, respectively. Their topographical profiles are shown in Fig. S8.

can explain the difference in albedo. Their mafic mineral abundances are also different (33.8 ± 9.9 vol % vs 25.4 ± 6.9 vol % CPX, 23.3 ± 5.9 vol % vs 30.1 ± 6.6 vol % OPX, 3.6 ± 2.8 vol % vs 0.9 ± 3.0 vol % OLV). According to the extracted spectra, both Southern Mare 1 and 2 are dominated by pyroxene (Fig. 3). The pyroxene in Southern Mare 2 may contain more Ca as suggested by the longer wavelengths of Band I and II absorptions (Klima et al., 2007).

According to our CSFD measurements, Southern Mare 1 and 2 have

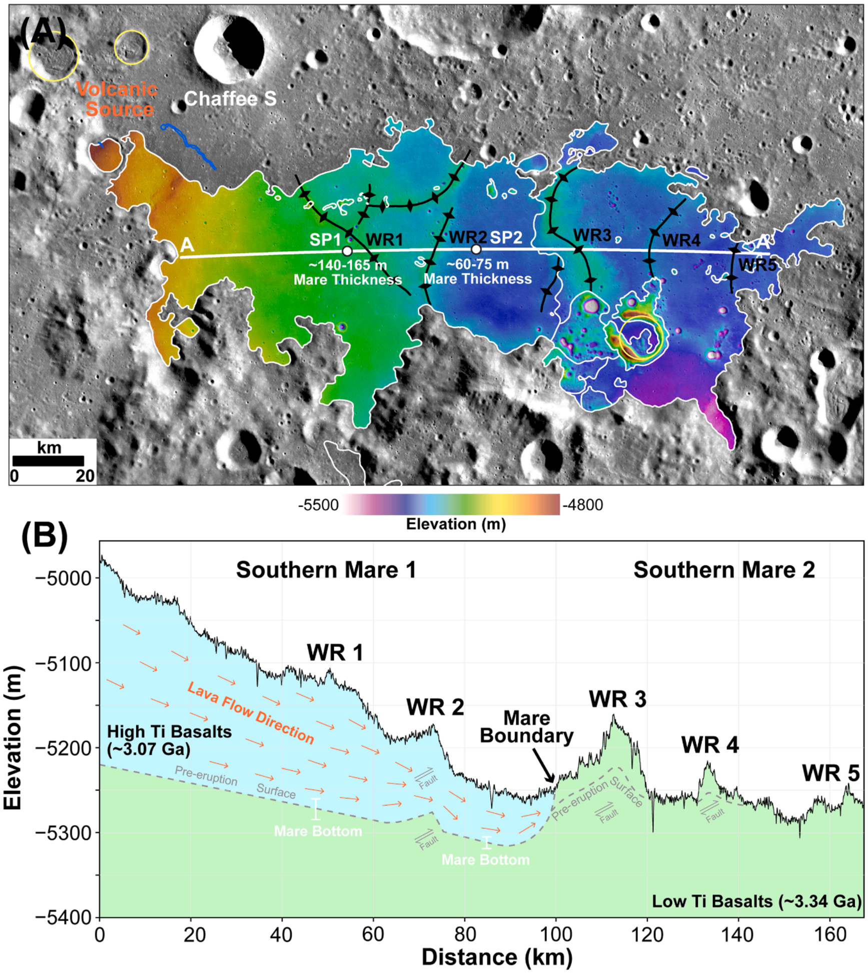

Fig. 5. Stratigraphy of the Southern Mare. (A) Topography and mare thickness of the Southern Mare. Yellow circles represent floor-fractured craters. Blue lines represent sinuous rilles. Black lines represent wrinkle ridges. The white line represents the topographic profile line (A-A') based on SLDEM2015. (B) Geological cross-section of the Southern Mare. Southern Mare 1 erupted from west close to Chaffee crater, closely following Southern Mare 2 and covered the west of Southern Mare.

AMAs of $3.07^{+0.07}_{-0.08}$ Ga and $3.34^{+0.04}_{-0.06}$ Ga, respectively. It suggests that the onset of Southern Mare 1 volcanism postdates that of Mare 2 but follows it very closely.

3.6. *Cryptomare White-Grissom*

Cryptomaria are ancient volcanic deposits obscured by highland ejecta (Whitten and Head, 2015). On the southern rim of the Apollo basin, there is a cryptomare identified previously by Whitten and Head (2015) and designated Cryptomare White-Grissom here, according to the name of two nearby craters (Fig. 6B).

Although the majority of Cryptomare White-Grissom has been buried by highland ejecta, a few post-formation craters punched through and excavated underlying ancient volcanic deposits. We labelled them as Type 1 Areas and the adjacent ejecta as the Type 2 Area (Fig. 6 CD). The Type 2 Area contains more highland felsic materials (13.1 ± 0.7 wt % FeO;1.4 ± 0.3 wt % TiO_2), with a PLG abundance much higher (63.8 ± 3.2 vol %, Table 1) than all mare units. According to the extracted spectra, the Type 2 Area has a pyroxene composition close to Fe-OPX (Fig. 3), unlike CPX-dominated mare basalts. In contrast, Type 1 Areas are more representative of obscured ancient volcanic deposits, mixed with few nonmare materials. It has a lower PLG (58.6 ± 9.0 vol %), but higher FeO (14.8 ± 0.8 wt %) and TiO_2 (2.1 ± 0.4 wt %) abundances than Type 2 Area. The pyroxene composition of the Type 1 Areas is more similar to mare units with a signature of low-Ca CPX (Fig. 3).

Our CSFD measurements on Cryptomare White-Grissom yielded an AMA of $4.05^{+0.01}_{-0.01}$ Ga, indistinguishable from the age of Apollo basin ($3.98^{+0.04}_{-0.06}$ Ga; Ivanov et al., 2018). No impact ejecta on cryptomare can be readily traced back to Apollo, indicating that cryptomare erupted closely following the Apollo impact and overlaying on its ejecta. Secondary craters from the Orientale basin (~3.80 Ga; Yue et al., 2020), were found on the Cryptomare White-Grissom (Guo et al., 2018). The Orientale ejecta is estimated to be ~70–100 m-thick in this area based on the power-law model of Fassett et al. (2011). Therefore, Cryptomare White-Grissom may have erupted between the Apollo and Orientale impacts; the Orientale basin impact contributes significant amounts of superposed ejecta on these cryptomaria.

3.7. *Floor-fractured craters*

Floor-fractured craters (FFCs) are a class of craters characterized by anomalously shallow floors with additional interior fractures and volcanic features (Schultz, 1976). Global investigation of LRO LOLA, LROC and GRAIL data suggest FFCs may be formed by shallow magmatic intrusion and uplift (Jozwiak et al., 2012). Applying higher-resolution TC images helped to identify at least 46 FFCs (Fig. 7F). All the recognized FFCs are located to the southwest part of the study area, among which FFC1 to FFC11 are within the Apollo basin.

According to the classification scheme of Jozwiak et al. (2012), FFCs in the study area were subdivided into 5 morphological classes, i.e. class 3, 4b, 4c, 5, and 6 (Fig. 7F). An example of each identified class is shown in Fig. 7A-E. Oppenheimer crater (FFC12, class 6, centered at 35.39°S,

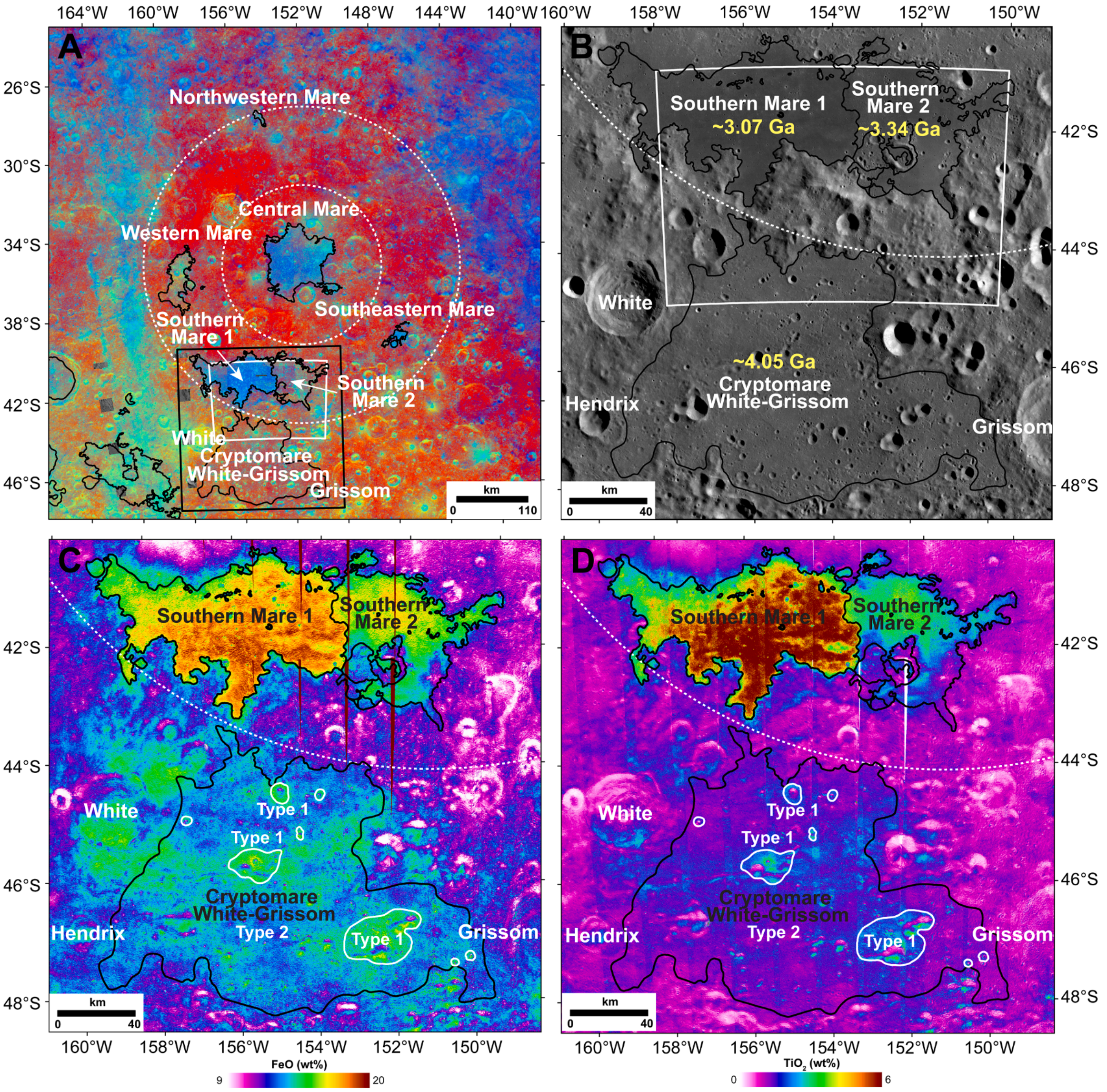

Fig. 6. Southern Mare and Cryptomare White-Grissom. (A) Mare units in the study area. The basemap is Clementine UVVIS color ratio map. (B) LRO WAC image. (C) Kaguya MI FeO abundance map. (D) Kaguya MI TiO_2 abundance map. Black lines represent mare and cryptomare boundaries. White lines represent type 1 cryptomare areas.

194.07°E) is the most prominent FFC to the west of Apollo basin, with a diameter of 206 km. Abundant concentric fractures are distributed close to its wall, together with seven pyroclastic vents (yellow triangles, Fig. 7E). There are five craters within Oppenheimer crater that appear to be FFCs. FFC1, just below the north rim of the Apollo basin, is the only one within the basin that has associated pyroclastic vents (yellow triangles, Fig. 7A). Anders X crater is a FFC (FFC9, class 5, centered at 39.72°S, 215.76°E), located just below the southeast rim of the Apollo basin. It displays radial and concentric fractures, with hummocky mounds in the west (Fig. 7D). Those mounds appear to extend to the west of Anders X crater through a breach in the crater rim.

4. Discussion

4.1. Evolution of Southern Mare basalts

CE-6 will most likely sample the mare basalts in the Southern Mare between the peak ring and rim crest of the Apollo basin (Zeng et al., 2023), therefore we focus on constructing its detailed eruption history and substructures (Fig. 5B). There were at least two episodes of mare eruptions in this region. The earliest volcanic activity occurred at ~3.34 Ga with low-Ti (3.2 wt %) composition, followed shortly by the high-Ti eruptions (6.2 wt %, ~3.07 Ga). Although low-Ti mare basalts are only observed in the current Southern Mare 2 region, we propose that it is distributed across the entire low topography region between the peak ring and rim crest of Apollo. Then, the relatively young high-Ti eruption obscured the low-Ti basalts in the west of the Southern Mare. A crater excavation technique was used to constrain the mare thickness of the superposed high-Ti basalts (Details in Text S2). By comparing the diameter of penetrating and non-penetrating craters, mare thicknesses for two spots (SP1 and SP2) on the topographic profile line of the Southern Mare (Fig. 5A) were obtained. SP1 to the west of WR1 has a high-Ti mare thickness of ~140–165 m; and SP2 between WR2 and WR3 has a high-Ti mare thickness of ~60–75 m. The mare thickness decreases from west to the east in Southern Mare 1, reflected in the trend of elevation.

The boundary between Southern Mare 1 and 2 correlates well with WR3. Considering that the formation of wrinkle ridge is a process associated with the gradual cooling of the Moon (Valantinas and Schultz, 2020), it is possible that WR3 started to form before the high-Ti

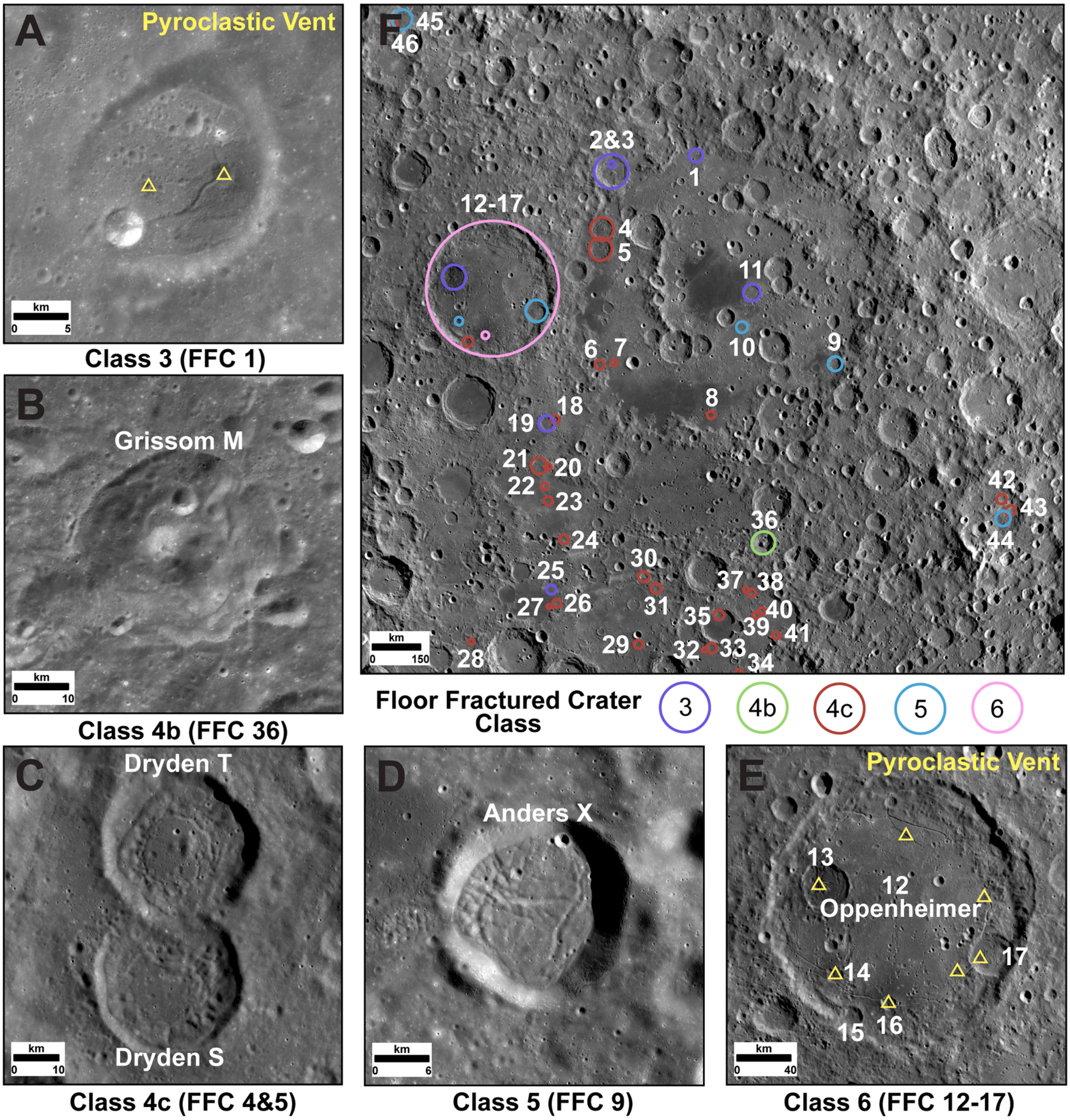

Fig. 7. Floor-fractured craters in the study area. (A-E) Examples of different classes of FFCs. (F) Distribution of FFCs and their morphological classes. Yellow triangles represent pyroclastic vents. The basemap of (A, B) are TC Ortho Map; the basemaps of other figures are LROC WAC images.

eruption. The high western part of Southern Mare 1 close to Chaffee S crater is the most probable lava source (Fig. 5A). This region displays abundant volcanic features, including floor-fractured craters and sinuous rilles, and even more may be buried by the ejecta from Chaffee S crater. When high-Ti lava erupted, it flowed from the west to the east with decreasing thickness, and finally encountering proto-WR3. Given typical lava flow eruption velocities, these flows are likely to have lacked sufficient velocity to overtop the ridge, and thus would pond behind proto-WR3 and then solidify to form Southern Mare 1. Subsequently, wrinkle ridges continued to develop to form the WR1-WR5 seen today.

The stratigraphy of the southern part of the Apollo basin is shown in Fig. 5B based on the regional volcanic/tectonic history. The low-Ti and high-Ti basalts occur together in the south of the Apollo basin, as is observed near the CE-5 site in northern Oceanus Procellarum (Qian et al., 2021). The CE-5 (5.0 wt % TiO_2) basalts have recently been interpreted to be evolved from a low-Ti source similar to the Apollo-12 basalts (Luo et al., 2023). Assessing the high-Ti basalts and their petrogenetic relationships to the low-Ti basalts in the CE-6 region should be a high priority for the analysis of the returned CE-6 samples.

4.2. *Long-lasting volcanism in the Apollo basin and lunar thermal evolution*

The duration of mare volcanism reflects the interior state of the Moon and its long-term thermal evolution (Head et al., 2023). Large-scale mare volcanism, as revealed by surface deposits, is first seen on the Moon in the form of cryptomaria with ages (>3.8 Ga), coincident with the major basin formation era (Whitten and Head, 2015). Being obscured by basin ejecta, cryptomaria distribution is limited, occupying only ~10 % area of all recognized mare deposits. Samples from cryptomaria have never been identified, although a few basaltic clasts in meteorites could represent ancient volcanism (e.g., Kalahari 009, 4.37 Ga; MIL 13317, 4.33 Ga; Snape et al., 2018). Young mare basalts are also rare on the Moon. After peaking in the Late Imbrian Epoch, lunar volcanism decreased significantly in the Eratosthenian Period and finally ceased at ~1.0 Ga (Hiesinger et al., 2011). Most of the Eratosthenian-aged young basalts are confined to the Procellarum KREEP Terrane (Hiesinger et al., 2011; Qian et al., 2023) and few occur on the farside (Haruyama et al., 2009; Pasckert et al., 2018).

Our CSFD measurements show that the study area in and around the Apollo basin has a long volcanic history (Table 1). A comparison of northeast SPA/Apollo basin mare basalt chronology and nearside mare basalt chronology is shown in Fig. 8. Cryptomare volcanism is the most ancient recorded volcanic activity in the area to the south of Apollo basin between White, Hendrix, and Grissom craters, with an approximate age of ~4.05 Ga (Fig. 8). Its primary composition is no longer discernable due to ejecta contamination and burial from the Orientale (~3.8 Ga) impact.

Subsequently, Imbrian-aged mare volcanism (~3.34 Ga) occurred in the southern part of the Apollo basin, where low-Ti (3.2 wt %) mare basalts erupted and covered the entire Southern Mare area (Fig. 5B). Immediately following this eruptive phase at ~3.07 Ga, high-Ti mare basalts (6.2 wt %) began to erupt in the west of the Southern Mare around Chaffee S crater, flowed east, and formed the current Southern Mare 1. The eastern part of the Southern Mare was not obscured or buried by the high-Ti basalts and remained exposed as the Southern Mare 2 unit. At ~2.72 Ga, high-Ti (6.2 wt %) volcanism initiated in the southeast of the Apollo basin (Fig. 8A).

Young Eratosthenian-aged (~2.12 Ga), low-Ti (3.2 wt %) volcanism then became active in the west of the Apollo Basin, superposed on the even lower-Ti (1.2 wt %) Imbrian-aged basalts. The majority of the Imbrian-aged basalts have been buried but the Dome 2 kipuka remains as an indicator of their presence (Fig. 4L). At ~2.01 Ga, high-Ti volcanism (6.5 wt %) was active again in the center of the Apollo basin (Fig. 8A). Because most of the volcanic features (sinuous rilles and volcanic mesas) within Central Mare are distributed in its northwest, southwest, and southeast parts, they may represent volcanically active spots where lava erupted and flowed into the interior of the basin. Volcanic mesas probably formed in a kipuka-controlled cooling processes because they are all associated with nonmare kipukas and have the same composition as the adjacent mare (Head and Ivanov, 2023). Finally, due to the secular cooling of the Moon, volcanic activity in the Apollo basin ceased. The last mare unit erupted at ~1.79 Ga in the Northwestern Mare, with low-Ti (2.2 wt %) composition (Fig. 8A). Large troughs were formed and may have deformed the surface of Northwestern Mare (Fig. 1B).

The mare units in the Apollo basin have also been dated by other studies (Greeley et al., 1993; Haruyama et al., 2009; Pasckert et al., 2018; Zeng et al., 2023) (Table S1). Thus, we derived model ages using the chronology function of Neukum et al. (2001) and the cumulative fitting method for direct comparison with Pasckert et al. (2018) (Table S2). Three recent studies (this study, Pasckert et al., 2018, and Zeng et al., 2023) all suggest the Apollo basin has a long volcanic history, from the Nectarian to Eratosthenian Periods. Earlier research by Greeley et al. (1993) suffered from an absence of high-resolution images as they themselves noted. Haruyama et al. (2009) did not subdivide Southern Mare into two mare units, therefore their age for Southern Mare may represent an average age of Southern Mare 1 and 2. The ages reported in our study, Pasckert et al. (2018), and Zeng et al. (2023) are closer to each other for the Imbrian-aged units (Southern Mare 1, 2) but differ for the younger ones. The difference in ages is, however, not surprising given the different crater counting areas selected (our crater counting areas are smaller) on different datasets (Fig. S5), as well as the use of different production and chronology functions with different fitting methods. Smaller areas examining smaller crater diameter ranges in higher resolution image data, such as in our study, allow the detection of younger, small-scale geological activities compared to studies examining larger crater diameters in lower resolution image data (e.g., Pasckert et al., 2018). Pasckert et al. (2015) also showed that smaller areas within a larger count area exhibit variations in age due to local geological processes, including resurfacing due to relatively large craters. Finally, slight differences between the fit *N(1)* values for surfaces with ages between ~1 and 3 Ga produce relatively larger differences in age, due to the flatness of the chronology functions in this age range (e.g., Hiesinger et al., 2023; Williams et al., 2018).

All in all, located in a transitional zone in the SPA basin both in crustal thickness (Wieczorek et al., 2013) and composition (Moriarty and Pieters, 2018), the Apollo basin displays a long-duration volcanic history (~2 Ga), from ~4.05 to ~1.79 Ga. Abundant mare deposits and features formed in the northwest, center, west, southeast, and south of the Apollo basin, and together additional information important in deciphering lunar volcanology in space and time (Fig. 8). These varied age basalts may be transported to the CE-6 landing site as impact ejecta and contained in the samples.

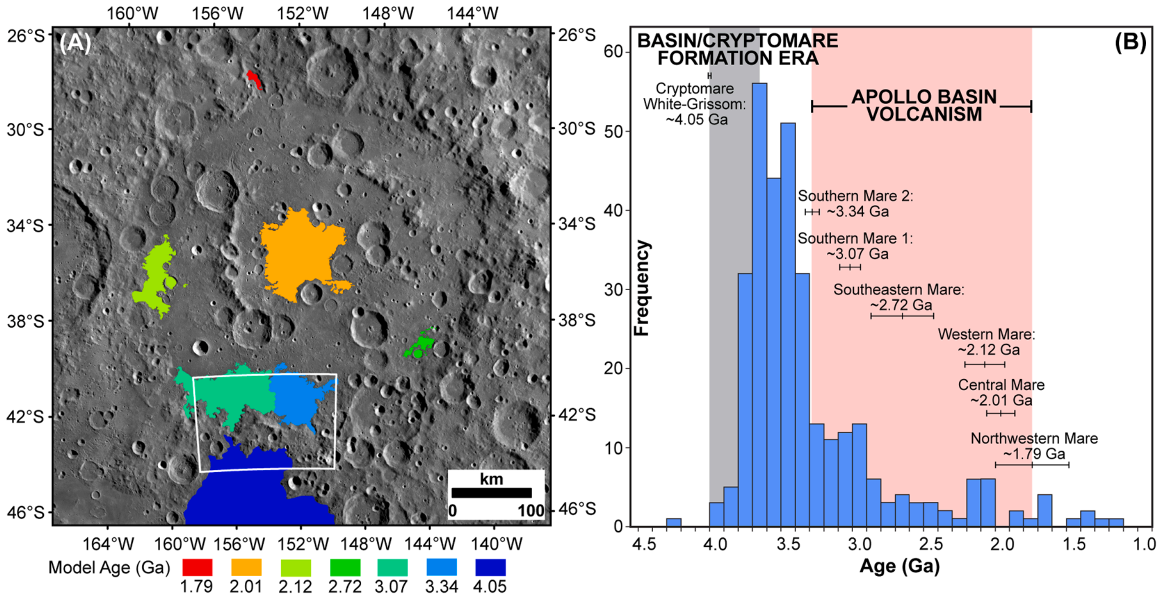

Fig. 8. Duration of mare volcanism in the Apollo basin and immediate surroundings. (A) Absolute model age of mare units (Table 1). The white box represents the CE-6 landing region. The basemap is a LROC WAC image. (B) Duration of mare volcanism in comparison with lunar mare flux based on Hiesinger et al. (2011) and Whitten and Head (2015).

4.3. Testing crustal thickness as a control on volcanic activity and assessing the nearside-farside asymmetry using Chang'e-6 basalts

Initially recognized by Luna 3 in 1959, the origin of nearside-farside asymmetry is one of the most fundamental unsolved lunar conundrum, clearly depicted by the mare volcanism distribution (Nelson et al., 2014; Whitten and Head, 2015). Crustal thickness is one of the key factors controlling the nature and distribution of lunar volcanic activities (Head and Wilson, 2017; Wilson and Head, 2017): rising basaltic magma is positively buoyant in the mantle and negatively buoyant in the anorthositic crust, therefore extrusion is favored in thin-crust and intrusion is favored in thick-crust. Located in the transitional zone from thin to thick crust in the northeast edge of SPA, the Apollo basin is an ideal place to test the effect of crustal thickness on the presence, abundance and nature of volcanic activity. In this study, crustal thickness derived from the GRAIL mission (Wieczorek et al., 2013) was utilized, overlain by compositional zones mapped by Moriarty and Pieters (2018) (i.e., SPACA, Mg-Pyroxene Annulus, and Heterogeneous Annulus), mare units and FFCs mapped here (Fig. 9A). SPACA is an acronym for the SPA Compositional Anomaly. The crust-mantle subsurface structure was reconstructed based on the above data across the center of Apollo basin (B-B', Fig. 9B).

The crustal thickness (Fig. 9A) of the region decreases towards the SPA center (53°S, 191°E; Garrick-Bethell and Zuber, 2009), due to the excavation and removal of a significant amount of crust. The compositional zones of SPA generally compare well with crustal thickness (SPACA 16 km, Mg-Pyroxene Annulus 20 km, and Heterogeneous Annulus 30 km, in average) from inside to outside. Outside SPA, the farside highland crust has a thickness of 40–60 km. In the study area, most of the mare units and FFCs are distributed within SPACA, fewer in the Mg-Pyroxene Annulus, only a few in Heterogeneous Annulus, and none in the primary highland crust.

The cross-section (Fig. 9B) even more clearly depicts the correlation of crustal thickness and mare volcanism. From west to east, crustal thickness maps from intermediate-thick (~18 km), thin (~5 km), and thick (~36 km) crust regions shaped by the SPA impact. In the intermediate-thick crust region, the Oppenheimer impact further removed the uppermost remaining crust and uplifted the mantle by ~5 km. Magmatic driving pressure (Wilson and Head, 2017) in intermediate-thick crust, combined with the effects of Oppenheimer crater breccia lens, caused the dike to stall underneath and spread laterally to form a sill, uplift the crater floor and form a floor-fractured crater (Jozwiak et al., 2012). A few small-scale dikes erupted from the sill and formed pyroclastic vents and basalts within the Oppenheimer

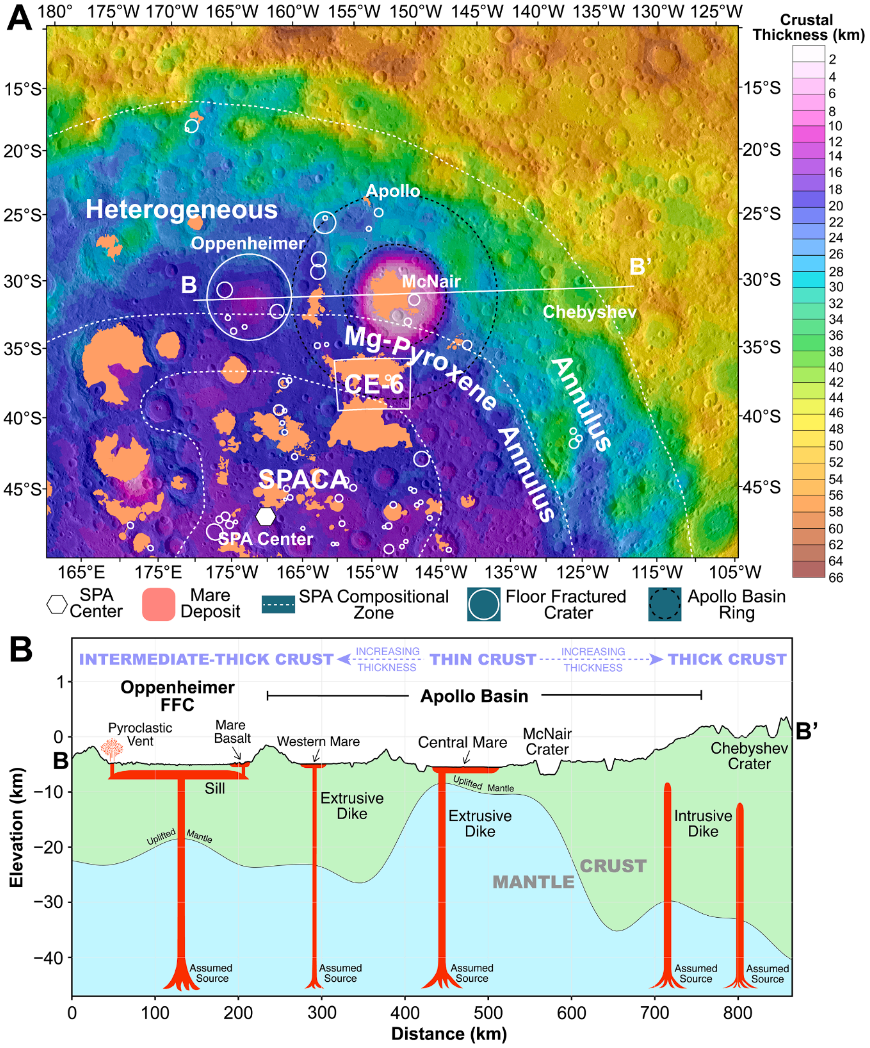

Fig. 9. Stratigraphy of the Apollo basin. (A) Crustal thickness of the northeast part of the SPA basin. The black dashed circles represent Apollo basin rings. The white circles represent floor-fractured craters. The white dashed lines indicate compositional zones of the SPA basin (Moriarty and Pieters, 2018). The red patches represent mare or cryptomare basalts (Nelson et al., 2014; Whitten and Head, 2015). The basemap is crustal thickness (Wieczorek et al., 2013) overlain on a LRO WAC image. (B) Geological cross-section of the northeast part of the SPA basin. Crustal thickness profile (B-B', white line) is based on Wieczorek et al. (2013).

crater. For the thin-crust region in the central Apollo basin, the upper crust was removed by the impact, and the mantle uplifted to only ∼5 km below the surface. Following magma generation in the deeper mantle, magma-filled cracks (dikes) rapidly propagated vertically through the mantle, penetrated the thin-crust and erupted directly to the surface, forming one of the largest farside mare patches. In contrast, for the thick-crust region, an area of thicker crust due to slumped SPA basin rim material and SPA ejecta, crustal thickness could reach ∼30 km. The absence of mare basalt surface deposits in the thick-crust areas is likely due to fact that dikes generated at depth in the mantle lack sufficient overpressure to penetrate the thick crust and reach the surface (Wilson and Head, 2017), and stall below the surface to form intrusive dikes.

In conclusion, our analyses support the hypothesis that crustal thickness is a significant control on the presence, abundance and style of lunar volcanism in the northeastern SPA basin, especially in the Apollo basin where CE-6 is targeted to land. Mare basalts exposed at the surface are the extrusive volcanic product formed volcanically from the generation of mantle partial melts, and their subsequent ascent and eruption, thus containing abundant information (temperature, elemental/mineralogical composition, pressure, and oxygen fugacity) on the lunar interior (Neal and Taylor, 1992). Detailed analyses of mare samples from the CE-6 landing site will help in our understanding of their petrogenesis, generation, ascent, and eruption. This in turn can help to know the nature of the farside mantle, and how it compares to that of the nearside, as we understand it based on the Apollo, Luna, and recent Chang'e-5 samples. It may finally resolve the question of whether crustal thickness controls volcanic activity and how and why the two hemispheres of the Moon apparently evolved so differently.

5. Conclusions

China's CE-6 mission, scheduled to launch in 2024, will be first lunar farside sample-return mission. The CE-6 landing site is within the SPA basin, in the southern part of the Apollo basin. It is highly likely that CE-6 will collect lunar basalts that have significant implications for the magmatic processes and the farside mantle properties. Therefore, we conducted this comprehensive study to characterize the volcanism of the Apollo basin and its surroundings. Located in the transitional zone at the inner edge of the SPA basin with variable crustal thickness and composition, we found that the Apollo basin has an extensive volcanic history dating from the Nectarian (∼4.05 Ga) to the Eratosthenian Period (∼1.79 Ga). Volcanic activity in the region was significantly influenced by crustal thickness variations, with thinning caused by the SPA and Apollo impacts. Dikes in intermediate-thickness crust (below Oppenheimer crater) tend to stall beneath the crater floor, spreading laterally to form a sill and an FFC; dikes below the crust thinned by Apollo basin event, reach directly to the surface and erupt to form widespread lava flows; and dikes in thick crust stall before being able to reach the surface and form basaltic dike intrusions. For the Southern Mare CE-6 candidate landing site, there are at least two episodes of eruptions. The earlier unit (∼3.34 Ga) has low-Ti composition and covered the entire topographically low region between the Apollo peak ring and basin rim. The later unit (∼3.07 Ga), with high-Ti composition, erupted from the western part of the Southern Mare close to Chaffee S crater and flowed east until encountering proto-wrinkle ridge (WR3). We present this analysis and synthesis as a framework for assessing and analyzing the samples planned to be returned by CE-6. These returned samples could help to answer questions about the evolution of high-Ti and low-Ti basalts, the influence of crustal thickness on lunar volcanism, and the most fundamental unsolved question of lunar science: What is the cause of the pronounced lunar nearside-farside asymmetry? Finally, to solve these listed scientific questions, we suggest CE-6 to sample high-Ti basalts in the Southern Mare 1, considering the potential importance of returned materials. In addition to the local high-Ti basalts, underlying Southern Mare 2 low-Ti basalts may also be excavated and mixed with soils at the landing site, as well as exotic materials transported by distant impacts, especially Chaffee S crater.

Data availability

LROC WAC data are available from LROC website (http://lroc.sese.asu.edu). Kaguya TC and MI data are available from SELENE Data Archive (https://darts.isas.jaxa.jp/planet/pdap/selene/). SLDEM2015, LOLA data, and Clementine false color map is available from USGS Astropedia (https://astrogeology.usgs.gov/search?pmi-target=moon). M^3 data is available from PDS Geosciences Node (https://pds-geosciences.wustl.edu/default.htm). CraterTools and Craterstats are available from Freie Universität Berlin (https://www.fu-berlin.de/en/sites/75seiten/index.html).

CRediT authorship contribution statement

Yuqi Qian: Data curation, Conceptualization, Investigation, Methodology, Validation, Visualization, Writing – original draft, Writing – review & editing. **James Head:** Conceptualization, Methodology, Visualization, Writing – original draft, Writing – review & editing. **Joseph Michalski:** Writing – review & editing, Conceptualization, Funding acquisition, Methodology, Resources, Supervision, Writing – original draft. **Xing Wang:** Writing – review & editing, Writing – original draft, Validation, Methodology, Investigation, Data curation. **Carolyn H. van der Bogert:** Writing – review & editing, Writing – original draft, Validation, Methodology. **Harald Hiesinger:** Writing – review & editing, Writing – original draft, Validation, Methodology. **Lingzhi Sun:** Writing – review & editing, Writing – original draft, Validation, Methodology. **Wei Yang:** Writing – review & editing, Writing – original draft, Validation. **Long Xiao:** Writing – review & editing, Writing – original draft, Validation. **Xianhua Li:** Writing – review & editing, Writing – original draft, Validation. **Guochun Zhao:** Writing – review & editing, Writing – original draft, Validation.

Declaration of competing interest

The authors declare that they have no known competing financial interests or personal relationships that could have appeared to influence the work reported in this paper.

Acknowledgments

This research is funded by Research Impact Fund project (R5043-19). JWH acknowledges support from Brown University; no outside funding was utilized. CHvdB and HH were funded by the German Aerospace Center (Deutsches Zentrum für Luft- und Raumfahrt) Project 50OW2001. ChvdB, HH, and LX are members of the Lunar Science Exploration Consortium supported by Sino-German Center Mobility Project M-016.

Supplementary materials

Supplementary material associated with this article can be found, in the online version, at doi:10.1016/j.epsl.2024.118737.

References

Barker, M.K., Mazarico, E., Neumann, G.A., Zuber, M.T., Haruyama, J., Smith, D.E., 2016. A new lunar digital elevation model from the Lunar Orbiter Laser Altimeter and SELENE Terrain Camera. Icarus 273, 346–355. https://doi.org/10.1016/j.icarus.2015.07.039.

Besse, S., Yokota, Y., Boardman, J., Green, R., Haruyama, J., Isaacson, P., Mall, U., Matsunaga, T., Ohtake, M., Pieters, C., Staid, M., Sunshine, J., Yamamoto, S., 2013. One Moon, many measurements 2: photometric corrections. Icarus 226, 127–139. https://doi.org/10.1016/j.icarus.2013.05.009.

Boardman, J.W., Pieters, C.M., Green, R.O., Lundeen, S.R., Varanasi, P., Nettles, J., Petro, N., Isaacson, P., Besse, S., Taylor, L.A., 2011. Measuring moonlight: an overview of the spatial properties, lunar coverage, selenolocation, and related Level

1B products of the Moon Mineralogy Mapper. J. Geophys. Res. Planets 116. https://doi.org/10.1029/2010JE003730.

Calzada-Diaz, A., Joy, K.H., Crawford, I.A., Nordheim, T.A., 2015. Constraining the source regions of lunar meteorites using orbital geochemical data. Meteorit. Planet. Sci. 50, 214–228. https://doi.org/10.1111/maps.12412.

Clark, R.N., Pieters, C.M., Green, R.O., Boardman, J.W., Petro, N.E., 2011. Thermal removal from near-infrared imaging spectroscopy data of the Moon. J. Geophys. Res. Planets 116. https://doi.org/10.1029/2010JE003751.

Fassett, C.I., Head, J.W., Smith, D.E., Zuber, M.T., Neumann, G.A., 2011. Thickness of proximal ejecta from the Orientale Basin from Lunar Orbiter Laser Altimeter (LOLA) data: implications for multi-ring basin formation. Geophys. Res. Lett. 38 https://doi.org/10.1029/2011GL048502.

Garrick-Bethell, I., Miljković, K., Hiesinger, H., van der Bogert, C.H., Laneuville, M., Shuster, D.L., Korycansky, D.G., 2020. Troctolite 76535: a sample of the Moon's South Pole-Aitken basin? Icarus 338, 113430. https://doi.org/10.1016/j.icarus.2019.113430.

Garrick-Bethell, I., Zuber, M.T., 2009. Elliptical structure of the lunar South Pole-Aitken basin. Icarus 204, 399–408. https://doi.org/10.1016/j.icarus.2009.05.032.

Greeley, R., Kadel, S.D., Williams, D.A., Gaddis, L.R., Head, J.W., McEwen, A.S., Murchie, S.L., Nagel, E., Neukum, G., Pieters, C.M., Sunshine, J.M., Wagner, R., Belton, M.J.S., 1993. Galileo imaging observations of lunar maria and related deposits. J. Geophys. Res. Planets 98, 17183–17205. https://doi.org/10.1029/93JE01000.

Green, R.O., Pieters, C., Mouroulis, P., Eastwood, M., Boardman, J., Glavich, T., Isaacson, P., Annadurai, M., Besse, S., Barr, D., Buratti, B., Cate, D., Chatterjee, A., Clark, R., Cheek, L., Combe, J., Dhingra, D., Essandoh, V., Geier, S., Goswami, J.N., Green, R., Haemmerle, V., Head, J., Hovland, L., Hyman, S., Klima, R., Koch, T., Kramer, G., Kumar, A.S.K., Lee, K., Lundeen, S., Malaret, E., McCord, T., McLaughlin, S., Mustard, J., Nettles, J., Petro, N., Plourde, K., Racho, C., Rodriquez, J., Runyon, C., Sellar, G., Smith, C., Sobel, H., Staid, M., Sunshine, J., Taylor, L., Thaisen, K., Tompkins, S., Tseng, H., Vane, G., Varanasi, P., White, M., Wilson, D., 2011. The Moon Mineralogy Mapper (M3) imaging spectrometer for lunar science: instrument description, calibration, on-orbit measurements, science data calibration and on-orbit validation. J. Geophys. Res. Planets 116. https://doi.org/10.1029/2011JE003797.

Guo, D., Liu, J., Head James, W., Kreslavsky, M.A., 2018. Lunar orientale impact basin secondary craters: spatial distribution, size-frequency distribution, and estimation of fragment size. J. Geophys. Res. Planets 123, 1344–1367. https://doi.org/10.1029/2017JE005446.

Hapke, B., 1981. Bidirectional reflectance spectroscopy: 1. Theory. J. Geophys. Res. Solid Earth 86, 3039–3054. https://doi.org/10.1029/JB086iB04p03039.

Haruyama, J., Matsunaga, T., Ohtake, M., Morota, T., Honda, C., Yokota, Y., Torii, M., Ogawa, Y., 2008. Global lunar-surface mapping experiment using the Lunar Imager/Spectrometer on SELENE. Earth Planets Space 60, 243–255. https://doi.org/10.1186/BF03352788.

Haruyama, J., Ohtake, M., Matsunaga, T., Morota, T., Honda, C., Yokota, Y., Abe, M., Ogawa, Y., Miyamoto, H., Iwasaki, A., Pieters, C.M., Asada, N., Demura, H., Hirata, N., Terazono, J., Sasaki, S., Saiki, K., Yamaji, A., Torii, M., Josset, J.L., 2009. Long-lived volcanism on the lunar farside revealed by SELENE Terrain Camera. Science 323, 905.

Head, J.W., Gifford, A., 1980. Lunar mare domes: classification and modes of origin. Moon Planets 22, 235–258. https://doi.org/10.1007/BF00898434.

Head, J.W., Ivanov, M.A., 2023. Mare mesas in mare fecunditatis: characteristics of a newly documented class of mare volcanic feature. In: The 14th Moscow Solar System Symposium. Presented at the The 14th Moscow Solar System Symposium, Moscow.

Head, J.W., Wilson, L., 2017. Generation, ascent and eruption of magma on the Moon: new insights into source depths, magma supply, intrusions and effusive/explosive eruptions (Part 2: predicted emplacement processes and observations). Icarus 283, 176–223. https://doi.org/10.1016/j.icarus.2016.05.031.

Head, J.W., Wilson, L., Hiesinger, H., van der Bogert, C., Chen, Y., Dickson, J.L., Gaddis, L.R., Haruyama, J., Jawin, E.R., Jozwiak, L.M., Li, C., Liu, J., Morota, T., Needham, D.H., Ostrach, L.R., Pieters, C.M., Prissel, T.C., Qian, Y., Qiao, L., Rutherford, M.R., Scott, D.R., Whitten, J.L., Xiao, L., Zhang, F., Ziyuan, O., 2023. Lunar mare basaltic volcanism: volcanic features and emplacement processes. Rev. Mineral. Geochem. 89, 453–507. https://doi.org/10.2138/rmg.2023.89.11.

Hiesinger, H., Head, J.W., Wolf, U., Jaumann, R., Neukum, G., 2011. Ages and stratigraphy of lunar mare basalts: a synthesis. Spec. Pap. Geol. Soc. Am. 477, 1–51. https://doi.org/10.1130/2011.2477(01.

Hiesinger, H., van der Bogert, C.H., Michael, G., Schmedemann, N., Iqbal, W., Robbins, S. J., Ivanov, B., Williams, J.P., Zanetti, M., Plescia, J., Ostrach, L.R., Head III, J.W., 2023. The lunar cratering chronology. Rev. Mineral. Geochem. 89, 401–451. https://doi.org/10.2138/rmg.2023.89.10.

Isaacson, P.J., Petro, N.E., Pieters, C.M., Besse, S., Boardman, J.W., Clark, R.N., Green, R. O., Lundeen, S., Malaret, E., McLaughlin, S., Sunshine, J.M., Taylor, L.A., 2013. Development, importance, and effect of a ground truth correction for the Moon Mineralogy Mapper reflectance data set. J. Geophys. Res. Planets 118, 369–381. https://doi.org/10.1002/jgre.20048.

Ivanov, M.A., Hiesinger, H., van der Bogert, C.H., Orgel, C., Pasckert, J.H., Head, J.W., 2018. Geologic history of the Northern Portion of the South Pole-Aitken Basin on the Moon. J. Geophys. Res. Planets 123, 2585–2612. https://doi.org/10.1029/2018JE005590.

Jolliff, B., Petro, N., Moriarty, D., Watkins, R., Head, J., Potter, R., 2021. Sample return from the Moon's South Pole-Aitken Basin. Bull. Am. Astron. Soc. 53 https://doi.org/10.3847/25c2cfeb.5309cd69.

Jolliff, B.L., Gillis, J.J., Haskin, L.A., Korotev, R.L., Wieczorek, M.A., 2000. Major lunar crustal terranes: surface expressions and crust-mantle origins. J. Geophys. Res. Planets 105, 4197–4216. https://doi.org/10.1029/1999JE001103.

Jozwiak, L.M., Head, J.W., Zuber, M.T., Smith, D.E., Neumann, G.A., 2012. Lunar floor-fractured craters: classification, distribution, origin and implications for magmatism and shallow crustal structure. J. Geophys. Res. Planets 117. https://doi.org/10.1029/2012JE004134.

Jutzi, M., Asphaug, E., 2011. Forming the lunar farside highlands by accretion of a companion moon. Nature 476, 69–72. https://doi.org/10.1038/nature10289.

Klima, R.L., Pieters, C.M., Dyar, M.D., 2007. Spectroscopy of synthetic Mg-Fe pyroxenes I: spin-allowed and spin-forbidden crystal field bands in the visible and near-infrared. Meteorit. Planet. Sci. 42, 235–253. https://doi.org/10.1111/j.1945-5100.2007.tb00230.x.

Kneissl, T., van Gasselt, S., Neukum, G., 2011. Map-projection-independent crater size-frequency determination in GIS environments—New software tool for ArcGIS. Planet Space Sci. 59, 1243–1254. https://doi.org/10.1016/j.pss.2010.03.015.

Lemelin, M., Lucey, P.G., Song, E., Taylor, G.J., 2015. Lunar central peak mineralogy and iron content using the Kaguya Multiband Imager: reassessment of the compositional structure of the lunar crust. J. Geophys. Res. Planets 120, 869–887. https://doi.org/10.1002/2014JE004778.

Luo, B., Wang, Z., Song, J., Qian, Y., He, Q., Li, Y., Head, J.W., Moynier, F., Xiao, L., Becker, H., Huang, B., Ruan, B., Hu, Y., Pan, F., Xu, C., Liu, W., Zong, K., Zhao, J., Zhang, W., Hu, Z., She, Z., Wu, X., Zhang, H., 2023. The magmatic architecture and evolution of the Chang'e-5 lunar basalts. Nat. Geosci. 16, 301–308. https://doi.org/10.1038/s41561-023-01146-x.

Michael, G.G., Kneissl, T., Neesemann, A., 2016. Planetary surface dating from crater size-frequency distribution measurements: poisson timing analysis. Icarus 277, 279–285. https://doi.org/10.1016/j.icarus.2016.05.019.

Michael, G.G., Neukum, G., 2010. Planetary surface dating from crater size–frequency distribution measurements: partial resurfacing events and statistical age uncertainty. Earth Planet Sci. Lett. 294, 223–229. https://doi.org/10.1016/j.epsl.2009.12.041.

Moriarty, D.P., Pieters, C.M., 2018. The character of South Pole-Aitken basin: patterns of surface and subsurface composition. J. Geophys. Res. Planets 123, 729–747. https://doi.org/10.1002/2017JE005364.

Neal, C.R., Taylor, L.A., 1992. Petrogenesis of mare basalts: a record of lunar volcanism. Geochim. Cosmochim. Acta 56, 2177–2211. https://doi.org/10.1016/0016-7037(92)90184-K.

Nelson, D.M., Koeber, S.D., Daud, K., Robinson, M.S., Watters, T.R., Banks, M.E., Williams, N.R., 2014. Mapping lunar maria extents and lobate scarps using LROC image products. In: Presented at the 45th Lunar and Planetary Science Conference, Lunar and Planetary Institute, Houston, p. Abstract #2861.

Neukum, G., Ivanov, B.A., Hartmann, W.K., 2001. Cratering records in the inner solar system in relation to the lunar reference system. In: Kallenbach, R., Geiss, J., Hartmann, William K (Eds.), Cratering records in the inner solar system in relation to the lunar reference system. Chronology and Evolution of Mars 55–86.

Neumann, G.A., Zuber, M.T., Wieczorek, M.A., Head, J.W., Baker, D.M.H., Solomon, S.C., Smith, D.E., Lemoine, F.G., Mazarico, E., Sabaka, T.J., Goossens, S.J., Melosh, H.J., Phillips, R.J., Asmar, S.W., Konopliv, A.S., Williams, J.G., Sori, M.M., Soderblom, J. M., Miljković, K., Andrews-Hanna, J.C., Nimmo, F., Kiefer, W.S., 2015. Lunar impact basins revealed by Gravity Recovery and Interior Laboratory measurements. Sci. Adv. 1, e1500852 https://doi.org/10.1126/sciadv.1500852.

Nozette, S., Rustan, P., Pleasance, L.P., Kordas, J.F., Lewis, I.T., Park, H.S., Priest, R.E., Horan, D.M., Regeon, P., Lichtenberg, C.L., Shoemaker, E.M., Eliason, E.M., McEwen, A.S., Robinson, M.S., Spudis, P.D., Acton, C.H., Buratti, B.J., Duxbury, T.C., Baker, D.N., Jakosky, B.M., Blamont, J.E., Corson, M.P., Resnick, J.H., Rollins, C.J., Davies, M.E., Lucey, P.G., Malaret, E., Massie, M.A., Pieters, C.M., Reisse, R.A., Simpson, R.A., Smith, D.E., Sorenson, T.C., Breugge, R.W.V., Zuber, M.T., 1994. The clementine mission to the moon: scientific overview. Science 266, 1835.

Ohtake, M., Haruyama, J., Matsunaga, T., Kodama, S., Morota, T., Yokota, Y., 2008. Scientific objectives and specification of the SELENE multiband imager. Adv. Space Res. 42, 301–304. https://doi.org/10.1016/j.asr.2007.04.041.

Ohtake, M., Takeda, H., Matsunaga, T., Yokota, Y., Haruyama, J., Morota, T., Yamamoto, S., Ogawa, Y., Hiroi, T., Karouji, Y., Saiki, K., Lucey, P.G., 2012. Asymmetric crustal growth on the Moon indicated by primitive farside highland materials. Nat. Geosci. 5, 384. https://doi.org/10.1038/ngeo1458 https://www.nature.com/articles/ngeo1458#supplementary-information.

Otake, H., Ohtake, M., Hirata, N., 2012. Lunar iron and titanium abundance algorithms based on SELENE (Kaguya) multiband imager data. 43rd Lunar Planet. Sci. Conf.

Pasckert, J.H., Hiesinger, H., van der Bogert, C.H., 2018. Lunar farside volcanism in and around the South Pole–Aitken basin. Icarus 299, 538–562. https://doi.org/10.1016/j.icarus.2017.07.023.

Pasckert, J.H., Hiesinger, H., van der Bogert, C.H., 2015. Small-scale lunar farside volcanism. Icarus 257, 336–354. https://doi.org/10.1016/j.icarus.2015.04.040.

Pieters, C.M., Boardman, J., Buratti, B., Chatterjee, A., Clark, R., Glavich, T., Green, R., Head, J., Isaacson, P., Malaret, E., McCord, T., Mustard, J., Petro, N., Runyon, C., Staid, M., Sunshine, J., Taylor, L., Tompkins, S., Varanasi, P., White, M., 2009. The Moon Mineralogy Mapper (M3) on Chandrayaan-1. Curr. Sci. 96, 500–505.

Pieters, C.M., Head III, J.W., Gaddis, L, Jolliff, B., Duke, M, 2001. Rock types of South Pole-Aitken basin and extent of basaltic volcanism. J. Geophys. Res. Planets 106, 28001–28022. https://doi.org/10.1029/2000JE001414.

Pieters, C.M., Staid, M.I., Fischer, E.M., Tompkins, S., He, G., 1994. A sharper view of impact craters from clementine data. Science 266, 1844.

Potter, R.W.K., Collins, G.S., Kiefer, W.S., McGovern, P.J., Kring, D.A., 2012. Constraining the size of the South Pole-Aitken basin impact. Icarus 220, 730–743. https://doi.org/10.1016/j.icarus.2012.05.032.

Potter, R.W.K., Head, J.W., Guo, D., Liu, J., Xiao, L., 2018. The Apollo peak-ring impact basin: insights into the structure and evolution of the South Pole–Aitken basin. Icarus 306, 139–149. https://doi.org/10.1016/j.icarus.2018.02.007.

Qian, Y., She, Z., He, Q., Xiao, L., Wang, Z., Head, J.W., Sun, L., Wang, Y., Wu, B., Wu, X., Luo, B., Cao, K., Li, Y., Dong, M., Song, W., Pan, F., Michalski, J., Ye, B., Zhao, Jiawei, Zhao, S., Huang, J., Zhao, Jiannan, Wang, J., Zong, K., Hu, Z., 2023. Mineralogy and chronology of the young mare volcanism in the Procellarum-KREEP-Terrane. Nat. Astron. 7, 287–297. https://doi.org/10.1038/s41550-022-01862-1.

Qian, Y., Xiao, L., Head, J.W., van der Bogert, C.H., Hiesinger, H., Wilson, L., 2021. Young lunar mare basalts in the Chang'e-5 sample return region, northern Oceanus Procellarum. Earth Planet. Sci. Lett. 555, 116702 https://doi.org/10.1016/j.epsl.2020.116702.

Robinson, M.S., Brylow, S.M., Tschimmel, M., Humm, D., Lawrence, S.J., Thomas, P.C., Denevi, B.W., Bowman-Cisneros, E., Zerr, J., Ravine, M.A., Caplinger, M.A., Ghaemi, F.T., Schaffner, J.A., Malin, M.C., Mahanti, P., Bartels, A., Anderson, J., Tran, T.N., Eliason, E.M., McEwen, A.S., Turtle, E., Jolliff, B.L., Hiesinger, H., 2010. Lunar reconnaissance orbiter camera (LROC) instrument overview. Space Sci. Rev. 150, 81–124. https://doi.org/10.1007/s11214-010-9634-2.

Schultz, P.H., 1976. Floor-fractured lunar craters. Moon 15, 241–273. https://doi.org/10.1007/BF00562240.

Smith, D.E., Zuber, M.T., Jackson, G.B., Cavanaugh, J.F., Neumann, G.A., Riris, H., Sun, X., Zellar, R.S., Coltharp, C., Connelly, J., Katz, R.B., Kleyner, I., Liiva, P., Matuszeski, A., Mazarico, E.M., McGarry, J.F., Novo-Gradac, A.M., Ott, M.N., Peters, C., Ramos-Izquierdo, L.A., Ramsey, L., Rowlands, D.D., Schmidt, S., Scott, V. S., Shaw, G.B., Smith, J.C., Swinski, J.P., Torrence, M.H., Unger, G., Yu, A.W., Zagwodzki, T.W., 2010. The lunar orbiter laser altimeter investigation on the lunar reconnaissance orbiter mission. Space Sci. Rev. 150, 209–241. https://doi.org/10.1007/s11214-009-9512-y.

Snape, J.F., Curran, N.M., Whitehouse, M.J., Nemchin, A.A., Joy, K.H., Hopkinson, T., Anand, M., Bellucci, J.J., Kenny, G.G., 2018. Ancient volcanism on the Moon: insights from Pb isotopes in the MIL 13317 and Kalahari 009 lunar meteorites. Earth Planet Sci. Lett. 502, 84–95. https://doi.org/10.1016/j.epsl.2018.08.035.

Sun, L., Lucey, P.G., 2021. Unmixing mineral abundance and Mg# with radiative transfer theory: modeling and applications. J. Geophys. Res. Planets 126, e2020JE006691. https://doi.org/10.1029/2020JE006691.

Valantinas, A., Schultz, P.H., 2020. The origin of neotectonics on the lunar nearside. Geology 48, 649–653. https://doi.org/10.1130/G47202.1.

Wang, X., Head, J.W., Qian, Y., Zhao, W., Liu, J., Gao, Y., Wu, B., 2024. In: . Lunar and Planetary Institute, Houston p. Abstract #1873.

Whitten, J.L., Head, J.W., 2015. Lunar cryptomaria: physical characteristics, distribution, and implications for ancient volcanism. Icarus 247, 150–171. https://doi.org/10.1016/j.icarus.2014.09.031.

Wieczorek, M.A., Neumann, G.A., Nimmo, F., Kiefer, W.S., Taylor, G.J., Melosh, H.J., Phillips, R.J., Solomon, S.C., Andrews-Hanna, J.C., Asmar, S.W., Konopliv, A.S., Lemoine, F.G., Smith, D.E., Watkins, M.M., Williams, J.G., Zuber, M.T., 2013. The crust of the Moon as seen by GRAIL. Science 339, 671. https://doi.org/10.1126/science.1231530.

Williams, J.P., van der Bogert, C.H., Pathare, A.V., Michael, G.G., Kirchoff, M.R., Hiesinger, H., 2018. Dating very young planetary surfaces from crater statistics: a review of issues and challenges. Meteorit. Planet Sci. 53, 554–582. https://doi.org/10.1111/maps.12924.

Wilson, L., Head, J.W., 2017. Generation, ascent and eruption of magma on the Moon: new insights into source depths, magma supply, intrusions and effusive/explosive eruptions (Part 1: theory). Icarus 283, 146–175. https://doi.org/10.1016/j.icarus.2015.12.039.

Yue, Z., Di, K., Wan, W., Liu, Z., Gou, S., Liu, B., Peng, M., Wang, Y., Jia, M., Liu, J., Ouyang, Z., 2022. Updated lunar cratering chronology model with the radiometric age of Chang'e-5 samples. Nat. Astron. 6, 541–545. https://doi.org/10.1038/s41550-022-01604-3.

Yue, Z., Yang, M., Jia, M., Michael, G., Di, K., Gou, S., Liu, J., 2020. Refined model age for Orientale Basin derived from zonal crater dating of its ejecta. Icarus 346, 113804. https://doi.org/10.1016/j.icarus.2020.113804.

Zeng, X., Liu, D., Chen, Y., Zhou, Q., Ren, X., Zhang, Z., Yan, W., Chen, W., Wang, Q., Deng, X., Hu, H., Liu, J., Zuo, W., Head, J.W., Li, C., 2023. Landing site of the Chang'e-6 lunar farside sample return mission from the Apollo basin. Nat. Astron. https://doi.org/10.1038/s41550-023-02038-1.

Zhang, N., Ding, M., Zhu, M.H., Li, Huacheng, Li, Haoyuan, Yue, Z., 2022. Lunar compositional asymmetry explained by mantle overturn following the South Pole–Aitken impact. Nat. Geosci. 15, 37–41. https://doi.org/10.1038/s41561-021-00872-4.

Zhou, C., Jia, Y., Liu, J., Li, H., Fan, Y., Zhang, Z., Liu, Y., Jiang, Y., Zhou, B., He, Z., Yang, J., Hu, Y., Liu, Z., Qin, L., Lv, B., Fu, Z., Yan, J., Wang, C., Zou, Y., 2022. Scientific objectives and payloads of the lunar sample return mission—Chang'E-5. Adv. Space Res. 69, 823–836. https://doi.org/10.1016/j.asr.2021.09.001.